1   **Calcite U-Pb dating of altered ancient oceanic crust in the North Pamir, Central Asia**

2   Johannes Rembe1, Renjie Zhou2, Edward R. Sobel1, Jonas Kley3, Jie Chen4, Jian-xin Zhao2, Yuexing Feng2,

3   Daryl L. Howard5

4   1   Institute of Geosciences, University of Potsdam, 14476 Potsdam-Golm, Germany

5   2   School of Earth and Environmental Sciences, The University of Queensland, St. Lucia QLD 4072,

6   Australia

7   3   Department of Structural Geology and Geodynamics, Georg-August-Universität Göttingen, 37077

8   Göttingen, Germany

9   4   State Key Lab. of Earthquake Dynamics, Xinjiang Pamir Intracontinental Subduction National Field

10   Observation and Research Station, Institute of Geology, China Earthquake Administration, X9GJ+RV

11   Chaoyang, Beijing, China

12   5   The Australian Synchrotron, 800 Blackburn Rd Clayton, VIC 3168, Australia

13   Correspondence to: Johannes Rembe, jrembe@uni-potsdam.de

14   **Abstract.** The North Pamir, part of the western syntax of the India-Asia collision zone, preserves remnants of a

15   poorly understood Paleozoic intra-oceanic subduction zone. To constrain the age of this ancient ocean floor, we

16   analyzed calcite phases in vesicular basalt and basaltic volcanic breccia with U-Pb geochronology using laser-

17   ablation inductively-coupled-plasma mass-spectrometry (LA-ICP-MS). Dating of radial-fibrous to equant spary

18   calcite yielded three meaningful Visean-Serpukhovian ages. REE + Y data reveal that the basaltic host rock of

19   the calcite and oxidizing seawater are major sources of trace elements during calcite precipitation. U-Pb ages

20   seem to be independent of REE + Y concentrations. Our results demonstrate the potential of calcite dating to

21   constrain the age of ancient ocean floors. We challenge the hypothesis that a continuous early Paleozoic Kunlun

22   Terrane extended from northern Tibet into the North Pamir.

23   **Summary.** Calcite is frequently formed during alteration processes in the basaltic, uppermost layer of juvenile

24   oceanic crust. Weathered oceanic basalts are hard to date with conventional radiometric methods. We show in a

25   case study from the North Pamir, Central Asia, that calcite U-Pb age data—supported by geochemistry and

26   petrological microscopy—has the potential to date sufficiently old oceanic basalts, if the time span between

27   basalt extrusion and latest calcite precipitation (~25 Ma) is considered.

28   **1   Introduction**

29   Constraining the timing of formation of ocean floor basalts is significant to develop models of various tectonic

30   processes given the voluminous occurrence of ocean floor basalts in ophiolites, sections of ocean plate

31   stratigraphy and exhumed subduction complexes, and remnants of island-arcs and oceanic plateaus in ancient

32   convergent margins. However, mafic volcanic rocks, in which zircons are sparse, are challenging to date with

33   radiometric methods. $^{40}Ar/^{39}Ar$ dating of separated phenocrysts or groundmass is frequently attempted (e.g.,

34   Waagstein et al., 2002; Heath et al., 2018). However, ocean floor alteration (OFA) often disturbs K-Ar isotopic

35   compositions by secondary potassium gain (Staudigel et al., 2013) or loss (Pringle, 2013), making $^{40}Ar/^{39}Ar$

dating more successful in providing high precision age data for fresh volcanic rocks but problematic if samples were affected by OFA.

Calcite veins and calcite-filled amygdules are commonly observed in submarine volcanic rocks. Studies show that calcite formation occurs during OFA by alkalinity-generating reactions, shortly after the eruption of lavas (e.g. Coogan and Gillis, 2018; Spivack and Staudigel, 1994; Coogan et al., 2016), driven by the infiltrating seawater and heat extraction from the oceanic crust. Such processes dominantly occur within ~25 Ma after rock consolidation (Coogan and Gillis, 2018). Therefore, dating the calcite phases in ocean floor volcanic rocks has the potential to constrain the timing of rock formation.

Calcite LA-ICP-MS U-Pb dating has been applied to a range of geological problems such as dating of deformation (e.g., Nuriel et al., 2019), diagenesis, and sedimentation (e.g., Godeau et al., 2018), especially since several international reference materials were established (Roberts et al., 2017; Rasbury et al., 2021). We present the first study on calcite LA-ICP-MS U-Pb dating of Paleozoic oceanic crust. Several types of calcite were dated from a volcanic sequence in the Carboniferous North Pamir arc (Figure 1, e.g., Bazhenov and Burtman (1982)). Calcite U-Pb ages are consistent with regional geological data and existing radiometric ages from correlative volcanic units. With additional petrographic and geochemical data, our work sheds light on the potential of calcite U-Pb dating on ancient ocean floor volcanics and allows us to place better constraints on tectonic models of the Pamir.

2   Geological background and motivation

The North Pamir magmatic arc formed during the subduction of the Paleo-Tethys oceanic lithosphere (e.g., Bazhenov and Burtman, 1982). It can be traced from the Chinese NE Pamir along strike into the Darvaz mountain range in the Gorno-Badakhshan province of Tadjikistan and further south into the Badakhshan province of Afghanistan (Figure 1). Outcrops in the Chinese Oytag and Gez valleys have been correlated with the South Kunlun Terrane in the north Tibetan West Kunlun by connecting ophiolitic sequences along the proposed Oytag–Kudi suture (e.g., Mattern et al., 1996). However, existing age dating reveals dissimilarities of key rock units in this suture in the West Kunlun compared to the North Pamir. The West Kunlun Kudi suture closed in the Silurian, as interpreted from zircon and monazite LA-ICP-MS U-Pb dating of amphibolite-facies rock (Zhang et al., 2018a). In contrast, the North Pamir magmatic arc, to which the mafic volcanic rocks and associated plagiogranites in the Oytag and Gez valleys are assigned, seems to be much younger. It consists of poorly dated mafic and intermediate volcanics, associated volcaniclastic rocks, and subordinate cherts. A series of leucogranites and granodiorites, that intruded the arc between 360 and 314 Ma, has been dated recently (Jiang et al., 2008; Kang et al., 2015; Rembe et al., 2021; Zhang et al., 2006). The Oytag suture itself is a small outcrop of altered ultramafic rocks in the Gez valley (Jiang, 1992). To date, no age data was presented for those rocks. The green color of the North Pamir arc volcanic rocks, however, implies thorough spilitization, making them unsuitable for $^{40}Ar/^{39}Ar$ dating. We propose that abundant calcite associated with spilitic basalts are a product of OFA, and that calcite ages can serve as a constraint on the formation of ocean floor. Specifically, they provide the possibility of directly dating OFA as a proxy for the emplacement of mafic volcanic rocks.

We conducted calcite dating based on detailed petrographic and geochemical observations in order to provide age constraints on the North Pamir arc volcanic rocks and test its correlation with the West Kunlun. For that

74 purpose, we sampled 4 specimens at 3 different localities in the Chinese Qimgan valley (Figure 1). Samples

75 17NP436a and 17NP436b are from the same locality (sample location at N 39° 18′ 27″, E 74° 51′ 32″) and

76 represent redeposited brecciated mafic volcanic rock with interstitial calcite cement that was formed during an

77 early phase of brecciation (Figure 2a–c). Samples 15NP236 (sample location at N 39° 18′ 18″, E 74° 51′ 30″)

78 and 15NP233 (sample location at N 39° 18′ 16″, E 74° 51′ 47″) are from two localities with amygdaloid-basalt,

79 where 15NP236 was taken from a pillow basalt. We investigated amygdules filled exclusively with calcite

80 (Figure 2e, f)

81 **3   Methods**

82 **3.1   Petrological microscopy, cathodoluminescence microscopy (CL) and X-ray fluorescence**

83 **microscopy (XFM)**

84 Petrographic thin sections of all samples were studied with conventional light microscopy and

85 cathodoluminescence microscopy (CL). Polished thin sections of all samples were prepared. CL imaging was

86 done using an Olympus BXFM-F microscope equipped with a Lumic hot-cathode electron source and a highly

87 sensitive Olympus XC10 camera at the University of Potsdam. We recognized well preserved primary features

88 (see Sect. 4.1), which were then identified on the rock chips prepared for laser ablation. Detailed sample

89 petrography raises the chances for robust, meaningful ages, as emphasized recently by Roberts et al. (2021).

90 High resolution reflected light images indicate the position of ablation spots in Appendix A.

91 Additionally, we examined sample 17NP436a with scanning X-ray fluorescence microscopy (XFM). A polished

92 slab parallel to the surface examined with LA-ICP-MS was prepared from the same rock chip. XFM maps were

93 collected at the XFM beamline at the Australian Synchrotron (Howard et al., 2020). The incident excitation

94 energy was 18.5 keV. Pixel size and dwell time per pixel are indicated in the figures in Appendix B.

95 **3.2   Laser-ablation inductively-coupled-plasma mass-spectrometry (LA-ICP-MS)**

96 Rock samples were processed at the School of Earth and Environmental Sciences, The University of

97 Queensland. Samples 15NP233 and 15NP236 were cut and mounted to round mounts with one-inch diameters

98 (Figure 2e, f), for samples 17NP436a and 17NP436b we used polished rock chips (Figure 2b, c). Samples

99 mounts were polished with standard polishing procedures and finished with a 0.25 micrometer diamond

100 suspension.

101 LA-ICP-MS U-Pb dating and geochemical analysis was performed at The University of Queensland following

102 methods in Su et al. (2020) and Yang et al. (2021). Laser ablation was achieved using an ASI RESOlution 193

103 ArF nm excimer laser system. Following evacuation of air, He carrier gas was introduced into the laser cell at a

104 flow rate of 0.35 l/min. 0.005 l/min of N_2 gas was also introduced to the laser cell to enhance the measurement

105 sensitivity. The gas mixture was then introduced into the plasma torch of a Thermo iCAP RQ quadruple ICP-MS

106 with 1.06 l/min Ar nebulizer gas. No reaction gas was employed. The laser was run with a 100 µm diameter

107 round spot at 10 Hz, with a measured instrument laser-fluence (laser pulse energy per unit area) of 2.5 J/cm^2. For

108 U-Pb dating, each spot had 8 s of background, 20 s of data acquisition, and 15 s of wash out. For trace elemental

109 analysis, each spot had 6 s of background, 25 s of data acquisition, and 10 s of wash out. Prior to data

3

110   acquisition, ICP-MS signals were optimized during tuning. For our session, ~950 kcps of ^{238}U counts and ~ 0.22

111   of $^{206}Pb/^{238}U$ were achieved for measuring NIST612 glass using line scans of 3 µm/s, 10 Hz, 50 µm round laser

112   pit, and 3 J/cm^2.

113   U-Pb isotopes for geochronology (^{206}Pb, ^{207}Pb, ^{208}Pb, ^{232}Th, and ^{238}U) were measured with the following dwell

114   times, ^{206}Pb (0.025 s), ^{207}Pb (0.055 s), ^{208}Pb (0.005), ^{232}Th (0.005 s), and ^{238}U (0.02 s). Both glass standard

115   NIST614 and matrix-matched calcite standards were measured, bracketing unknown spots. NIST614 glass was

116   used for correction of $^{207}Pb/^{206}Pb$ fractionation and instrument drift in the $^{238}U/^{206}Pb$ ratio (Woodhead and Hergt,

117   2001). Raw data were processed using Iolite software v3.64 (Paton et al., 2011). After the initial correction, a

118   matrix-matched calcite reference material of known age was used for further correction of matrix-related mass

119   bias impacting the measured $^{238}U/^{206}Pb$ ratios, following the approach described elsewhere, as summarized in

120   Yang et al. (2021). We used a cross-calibrated in-house calcite reference material AHX-1D and PTKD-2 and an

121   international reference material WC-1 (Roberts et al., 2017) in our laser ablation session. The accuracy of

122   unknown spots is checked by measuring WC-1 and PTKD-2 as monitoring standards. For WC-1 we obtained an

123   age of 251 ± 1 Ma (2 σ), consistent with the recommended age of 254.4 ± 6.4 Ma (Roberts et al., 2017). The in-

124   house PTKD-2 standard gave an age of 154 ± 3 (2σ), consistent with our recommended age of 153.7 ± 1.7 Ma

125   (2σ), calibrated by isotope dilution. Therefore, we note that the accuracy for our measurements can be

126   calculated as 1.5 % for WC-1 and 0.3 % for PTKD-2. Uncertainty propagation was done according to the

127   principles defined by Horstwood et al. (2016). We present two age uncertainties as ±α/β (2σ), were α is without

128   propagated systematic uncertainties, and β is with propagated systematic uncertainties. We propagated our

129   analytical errors (typically <5% (2σ) on $^{238}U/^{206}Pb$ ratios) by incorporating ^{238}U decay constant error, long-term

130   variance of the reference materials $^{238}U/^{206}Pb$ ratios in the lab, and the analytical error of the monitor standard.

131   This resulted in a total propagated systematic uncertainty of 4.6% (2σ) into the analytical error.

132   Trace elemental analysis was conducted in the same ablation areas as the U-Pb spots but without overlapping

133   with U-Pb spots. Prior to data acquisition, ICP-MS signals were optimized during tuning while the oxide

134   production rate was controlled to be as low as possible. Our session was run when ThO/Th ratio was <0.002 for

135   measuring NIST612 glass using line scans of 3 µm/s, 10 Hz, 50 µm round laser pit, and 3 J/cm^2. ^{43}Ca was

136   measured as an internal standard. Data reduction was conducted using the Iolite software v3.64 (Paton et al.,

137   2011) with the Trace Element data reduction scheme. All reported concentrations were after international

138   standardization using Ca (Ca = 40.1 %).

139   **4   Results**

140   **4.1   Petrography and calcite occurrences**

141   In the Chinese Qimgan valley, basaltic to andesitic volcanic rocks contain large amounts of calcite in amygdules,

142   in between single lava pillows, and volcanic breccia layers (Figure 2 and Appendix A). Two samples, 15NP233

143   and 15NP236, are altered amygdaloid-basalts with published geochemistry (Supplementary Table 1, Rembe et

144   al., 2021). Samples 17NP436a and 17NP436b are from a volcanic breccia, rich in calcite cement fragments and

145   calcite-overgrown, angular volcanic rock fragments. The samples were collected from 3 localities, whereby

146   17NP436a and 17NP436b are from the same locality.

147 Amygdules in samples 15NP233 and -236 show one generation of spary or botryoidal calcite with typical

148 sweeping extinction under cross-polarized light (Figure 3a, b). Sample 15NP233 has vesicles up to 5 mm in

149 diameter filled exclusively with calcite. Sample 15NP236 has much smaller vesicles, around 1 mm in diameter,

150 filled with either calcite or zeolite. Both samples show high "Loss on Ignition" (LOI) values and anomalous

151 major element values for whole rock geochemistry, accounting for high secondary, volatile rich mineral content

152 (Supplementary Table 1). No fractures or veins cut across amygdules in these samples.

153 In samples 17NP436a and b, fracture and pore space in basaltic rock fragments shows multiple calcite

154 generations (Figure 3c, d). Most calcite formed prior to deposition of the breccia. Specifically, isolated cement

155 fragments are fully embedded in a fine-grained matrix (e.g., in sample 17NP436b). They may have formed in

156 fractures of a volcanic edifice and were redeposited after its collapse. In some cases, calcite cement is still

157 attached to the basaltic clasts and a series of 4 consecutive mineralization phases can be recognized (numbered 1

158 to 4 in Figure 3d, schematically depicted in Figure 3e-g). Some of the volcanic rock fragments show an early,

159 hydrothermal clay layer (Figure 3c and phase 1 in Figure 3d). The rock fragments—or if present, the clay

160 coatings—are overgrown by a first generation of radial-fibrous calcite. Larger voids are filled with late, equant

161 calcite (phase 2 and 3 in Figure 3d). The early, medium to coarse spary calcite cements (2 and 3 in Figure 3d)

162 and the matrix are crosscut by fine-sparitic calcite filled fissures (4 in Figure 3d) The fissures are distinguishable

163 from the spary calcite in transmitted and reflected light and were avoided during ablation.

164 Cathodoluminescence microscopy imaging reveals fibrous botryoidal textures of the vesicle filling calcite of

165 samples 15NP233 and 15NP236. They usually show no luminescence or a zonation of dull-yellowish and non-

166 luminescent fringes (Figure 4a,b). Bright yellow luminescence irregularly occurs along the rims of the vesicles.

167 Secondary fractures, crosscutting the vesicular fabric were not observed. We prepared slides from the rock chips

168 analyzed with LA-ICP-MS of samples 17NP436a and 17NP436b (Figure 4c-f). The basalt breccia samples

169 17NP436a and 17NP436b show non-luminescent to dull yellow luminescent spary calcite. Bright yellow

170 luminescence was observed along hairline subzones, which are interpreted as grain boundaries. The largely non-

171 luminescent spary calcite fragments stand out against the yellow luminescent altered volcaniclastic matrix.

172 Matrix and spary calcite fragments are intersected by bright-yellow, late-stage calcite (phase 4 in Figure 3d)

173 filled fractures (e.g., Figure 4c). They are well visible in transmitted and reflected light and were avoided during

174 ablation.

175 In order to better understand calcite phases, we further study 17NP436a with high-resolution synchrotron X-ray

176 fluorescence mapping (Howard et al., 2020), following methods described in Vanghi et al. (2019). Sr maps show

177 elevated concentration for the phase 2 and 3 calcite and much lower content in fissure filling calcite phase 4,

178 suggesting different geochemical regimes (Appendix B).

179 **4.2   LA-ICP-MS U-Pb Dating**

180 Four samples from three field sites were prepared for analysis. We obtained data from 839 single spots from 18

181 laser ablation areas (Appendix A), 3–6 ablation areas per sample (Figure 5, Figure 6), data table in

182 Supplementary Table 2. For age calculation we used the IsoplotR program (Vermeesch, 2018) version 3.5

183 running in R version 3.6.0. Ages are calculated for individual ablation areas by linear regression in a Tera–

184   Wasserburg plot. From the 839 single spot ablation data only 16 had to be omitted due to U content below

185   detection limit.

4.2.1   17NP436a

187   Six ablation areas were targeted in basalt breccia sample 17NP436a (Figure 5a-f). They are placed on isolated

188   coarse-sparitic, equant calcite cement fragments (areas A, C, D, E) and coarse-sparitic radial-fibrous to equant

189   calcite cement still connected to their basaltic substratum (areas B, F). Propagated errors are generally small

190   (~5%) and MSWD values are low to moderate. Area A is an isolated fragment of coarse-spary cement (Figure

191   4c) and yielded a lower intercept age of $331 \pm 2/15$ Ma (MSWD = 1.7) calculated from 119 single spot data

192   points. Eighty-two ablation spots yielded a lower intercept age of $324 \pm 4/16$ Ma (MSWD = 2.3) for Area B.

193   Sixty-four ablation spots gave a lower intercept age of $308 \pm 7/16$ Ma (MSWD = 2.5) for Area C. Area D gave a

194   similar lower intercept age of $307 \pm 6/15$ Ma (MSWD = 4.2, n = 40). Area E gave a rather low age of $298 \pm$

195    $10/17$ Ma with an elevated MSWD of 4.7, defined by 37 ablation spots. Sixty-one ablation spots on area F

196   (Figure 4f) defined a lower intercept age of $304 \pm 7/16$ Ma (MSWD = 3.5).

4.2.2   17NP436b

198   In basalt breccia sample 17NP436b, 4 ablation areas were targeted (Figure 5g-j). They are placed on isolated

199   coarse-sparitic, equant calcite cement fragments. Propagated errors are generally small (~5%) and MSWD values

200   are low to moderate. Area A (Figure 4d) yielded a lower intercept age of $339 \pm 6/17$ Ma (MSWD = 1) defined by

201   38 ablation spots. Area B yielded a lower intercept age of $322 \pm 3/15$ Ma (MSWD = 4.8) defined by 47 ablation

202   spots. Twenty-nine laser spots on area C (Figure 4e) yielded a lower intercept age of $328 \pm 4/16$ Ma (MSWD =

203   1.7). Twenty-three ablation spots gave a lower intercept age of $316 \pm 9/17$ Ma (MSWD = 2.4).

4.2.3   15NP236

205   Five ablation areas were targeted in vesicular basalt sample 15NP236 (Figure 6a-e). Each ablation area

206   represents one calcite filled vesicle. Due to the small vesicles, only few spots were placed per area. Propagated

207   errors are moderate to large (6-36%) and MSWD values are low to moderate. Area A yielded a lower intercept

208   age of $351 \pm 29/33$ Ma (MSWD = 2.2) defined by 14 single ablation spots. Fifteen ablation spots on area B gave

209   a lower intercept age of $306 \pm 64/65$ Ma with a low MSWD of 1.4. Ten spots on area C gave an age of $350 \pm$

210    $15/22$ Ma (MSWD = 2.2). Area D yielded a very young age of $206 \pm 73/73$ Ma (MSWD = 0.84) defined by 10

211   ablation spots. A similarly young age of $272 \pm 57/58$ Ma (MSWD = 4.3) was defined by 18 laser spots for area

212   E.

4.2.4   15NP233

214   Three ablation areas were placed on calcite in three filled vesicles in sample 15NP233 (Figure 6f-h). Propagated

215   errors are small (~5%) and MSWD values are moderate. Area A gave an age of $324 \pm 4/16$ Ma (MSWD = 2.4)

216   defined by 60 ablation spots. Ninty-nine ablation spots on area B yielded a similar age of $327 \pm 5/16$ Ma

217   (MSWD = 2.5). Fifty-eight ablation spots on area C gave a slightly higher age of $337 \pm 7/17$ Ma (MSWD =9.8).

4.3   LA-ICP-MS Geochemistry

For each laser ablation area, we measured Ca, Mn, Sr, Zr, Ba and REE + Y geochemical data (a total of 380 single spot analyses) using LA-ICP-MS (data in Supplementary Table 3). Calcite REE patterns normalized to chondrite (Boynton, 1984) are mostly flat to slightly "U" shaped (Appendix C). REE content of the vesicle-hosted calcite is higher (61 ppm mean total REE content in sample 15NP233, 59 ppm in sample 15NP236) compared to the breccia calcite cement (8 ppm in 17NP436a and 12 ppm in 17NP436b). LREE are enriched over MREE (La_n/Sm_n) and negatively correlate with enriched MREE over HREE values (Dy_n/Yb_n) in all samples. The vesicle filling calcite shows both positive and negative Ce/Ce* values between 0.75 and 1.41, the breccia calcite cement shows negative values between 0.18 and 0.92. Negative Ce anomalies are usually associated with oxidizing conditions producing Ce^{4+} instead of Ce^{3+} (e.g., Alibo and Nozaki, 1999). We observe positive to slightly negative Gd anomalies (Gd/Gd* = $Gd_n/sqrt(Eu_n \times Tb_n)$; Figure 7a). Positive Y_n/Ho_n anomalies are common (Figure 7b). Negative Ce/Ce* and Eu/Eu* anomalies together with higher Gd/Gd* and Y_n/Ho_n in the calcite cement of the volcanic breccia are interpreted to reflect a stronger influence of infiltrating seawater (Ce/Ce* = $Ce_n/sqrt(La_n \times Pr_n)$; Eu/Eu* = $Eu_n/sqrt(Sm_n \times Tb_n)$).

5   Discussion

5.1   Calcite age data and its significance

In newly formed submarine volcanic rocks, calcite formation marks the phase of alkalinity-generating reactions. Alkalinity describes the acid neutralizing capacity by formation of alkali and alkaline earth metal ion species during rock weathering (e.g., Spivack and Staudigel, 1994). This is crucial for interpreting OFA calcite U-Pb ages, implying that these ages should be no older than the "true" rock formation age. High temperature hydrothermal alteration is also a common phenomenon for submarine volcanic environments. This is, in contrast, restricted to discrete zones, such as veins, shear zones, and hydrothermal upflow zones (Harlov and Austrheim, 2013; Honnorez, 2003). It changes the mineral composition of the volcanic host rock completely, such that primary igneous textures are obliterated (e.g. epidosites, Honnorez, 2003). Such rock types must be avoided as they are unlikely to produce ages related to OFA. By dating isolated calcite, far from hydrothermal upflow zones, we determine the age range of OFA occurring shortly after rock consolidation. This gives a first order minimum age estimate for ocean floor formation, if not the actual age of formation. This must not be mistaken with the radiometric ages of the volcanic rock itself (e.g., ages of zircon U-Pb dating).

We observed one botryoidal to spary calcite phase in the vesicular basalts (Figure 3a, Figure 4a, b). Four stages of mineralization were observed in the basaltic breccia: (1) hydrothermal clay, (2) radial-fibrous calcite, (3) coarse equant-spary calcite and (4) fissure filling calcite crosscutting the entire fabric (Figure 3b-g). The presence of radial-fibrous and sparry, equant calcite crystals is typical of continuous calcite precipitation in a porous substratum (Gonzalez and Carpente, 1992). In a first phase, radial-fibrous calcite grows along the wall of the voids and successively reduces the porosity of the substratum, thereby hindering fluid flow. This reduces the calcite precipitation rate and the amount of nucleation, leading to larger, equant calcite crystals in the center of the voids. This model can be adopted for a first calcite phase (2 and 3 in Figure 3d). As the radial-fibrous and the equant calcite growth reflects one process, both calcite phases were chosen for ablation. The phase 4 fine-sparitic

filled fissures are interpreted to reflect a later tectonic event, expressed by differential stress, pressure solution

and reprecipitation of calcite in open joints (Figure 3g).

To explore the geologic significance of our age data, we first applied a very conservative filter closely examining

ages with MSWD < 2 and 2σ-error < 10%, as their isotope ratios are most likely measured from single

homogenous domains (e.g., Lan et al. (2022)). Subsequently, we also discuss all ages for a full view on the age

spectrum.

Our samples show generally a low variability in ablation area ages and initial lead values (Figure 5 and Figure

6). 2σ-errors with propagated systematic uncertainties are typically around 5%, only vesicular basalt sample

15NP236 shows high 2σ-errors. However, multi-stage calcite formation and possible subsequent alteration lead

to MSWD values above two and elevated age errors. Primary calcite was eventually affected by alteration and

crystallization of calcite with deviant chemistry even within microscopically identified seemingly homogenous

phases (e.g. phase 2 and 3 in Figure 3d). This is made visible by CL imaging of yellow-luminescent subzones

penetrating non-luminescent phase 2 and 3 calcite zones in Figure 4f. However, ablation spots placed on ablation

areas 17NP436a_A, 17NP436b_A and 17NP436b_C largely fall on what we interpret as phase 2 and 3, radial-

fibrous to equant calcite, characterized by non-luminescence (Figure 4c-e). The lower intercept ages are 331 ±

2/15 Ma (17NP436a_A), 339 ± 6/17 Ma (17NP436b_A) and 328 ± 4/16 Ma (17NP436b_C), which consistently

constraints the volcanic breccia to the Visean-Serpukhovian boundary. All ablation areas of basalt breccia

samples 17NP436a and 17NP436b and vesicular basalt sample 15NP233 overlap within propagated 2σ-errors.

Their scatter reflects either the mixed ages of multiple calcite formation events during the late Mississippian to

Pennsylvanian which cannot be resolved, or minor isotope disturbance (by heating and/or fluid flow) during a

much younger event. Vesicular basalt sample 15NP236 yielded less defined regressions, thus high age errors,

caused by the small spread of the limited number of ablation spots. However, two ablation areas 15NP236_B and

15NP236_D gave MSWD values of 1.4 and 0.84 respectively, while yielding much different lower intercept

ages. 15NP326_B gave an age of 306 ± 64/65 Ma, which overlaps with the ages of 15NP326_A (351 ± 29/33

Ma, MSWD = 2.2) and 15NP326_C (350 ± 15/22 Ma, MSWD = 2.2). 15NP236_D gave an age of 206 ± 73/73

Ma, which is apparently younger. This leads us to conclude, that Carboniferous primary ages were affected by

young events causing isotope disturbance and shift of the apparent, yet mixed ages towards younger values. This

might be true to a limited degree for all samples with MSWD > 2.

Calcite ages are consistent with published radiometric ages of correlative rock units in the North Pamir arc,

including two hornblende ^{40}Ar/^{39}Ar ages of ~350 Ma from a meta-andesite, zircon U-Pb ages of ~329 Ma from

felsic to intermediate volcanics in Altyn Darya valley (Schwab *et al.*, 2004), and zircon U-Pb ages of ~360 to

314 Ma from island arc granites (Ji et al., 2018; Rembe et al., 2021) (Figure 8). All these ages are interpreted by

the aforementioned authors to be primary magmatic ages and reflect the age of emplacement of those units.

5.2   Calcite REE + Y geochemistry

Whole rock geochrmical data of altered basalt has a flat C1-normalized REE pattern (Boynton, 1984), implying

an intra-oceanic arc origin (Jiang et al., 2008; Rembe et al., 2021). We suggest a possible control of the basalt

geochemistry on calcite REE patterns; any process altering this signal would significantly change the calcite

REE pattern (Debruyne et al., 2016).

293 REE partition coefficients between aqueous solution and precipitating calcite have been studied by experiments

294 (e.g., Perry and Gysi, 2018; Voigt et al., 2017), suggesting that variable physicochemical conditions could lead

295 to strongly differing integration of rare earth elements into the calcite lattice. We show that calcite cements of

296 samples 17NP436a and b are distinguishable from vesicle fillings in samples 15NP233 and -236 (Figure 7a, b).

297 Calcite must be the major REE + Y sink as our samples do not show any intergrowing, co-precipitated mineral

298 phase. The dominance of calcite hints at precipitation from CO_2-rich seawater derived hydrothermal fluids under

299 low temperature conditions (Talbi and Honnorez, 2003; Honnorez, 2003). This happened in the upper few 100

300 meters of the oceanic crust. We assume a low mineralization temperature. Under this condition, Eu is trivalent

301 and negative Eu/Eu* is directly inherited from the fluid reservoir (Debruyne et al., 2016). Pronounced negative

302 Ce/Ce* values are a typical inherited signal of oxidizing seawater (e.g., Alibo and Nozaki, 1999); in correlation

303 with increasing Y_n/Ho_n values, they trace back to oxidative sorption by Fe-Mn O(OH) species (Debruyne et al.,

304 2016). Positive Gd/Gd* values may be interpreted as a seawater signal (e.g., Baar et al., 1985). However,

305 markedly positive Gd anomalies together with positive Y_n/Ho_n values are less commonly reported. Similar

306 features were observed for high salinity waters of the Jordan graben lakes (e.g., Möller et al., 2007). Because

307 ocean floor aquifer porosities are highly heterogenous (e.g., Fisher and Becker, 2000), the higher porosity of

308 volcanic breccias 17NP436a and 17NP436b may have promoted seawater infiltration, leading to lower REE

309 concentrations and more pronounced Ce/Ce*, Eu/Eu*, Gd/Gd* and Y_n/Ho_n anomalies compared to amygdaloidal

310 basalt samples. We note, that Gd anomalies strongly correlate with REE concentration. Although, LA-ICP-MS

311 data acquisition was done according to international standards, we cannot completely exclude the possibility of

312 polyatomic interference of the measured ^{157}Gd isotope with $^{141}Pr^{16}O^+$ (May and Wiedmeyer, 1998).

5.3 Implications on tectonic models of the Pamir

314 The results from petrological thin section examination, showing primary calcite fabrics, together with LA-ICP-

315 MS trace element geochemistry, which reflect sea water infiltration, typical for OFA, are major arguments for

316 preserved, primary U-Pb isotopic ratios. Our studies constrain the arc volcanic rocks in the NE Pamir to Middle-

317 Upper Mississippian (Visean-Serpukhovian) (Figure 8), significantly younger than correlative lithologies in the

318 West Kunlun, which are dated to the Cambrian (e.g. Yixieke dacite, Xiao et al. (2005), Kudi ophiolite, Wang et

319 al. (2021)). The results carry significant implications for the interpretation of Mesozoic and Cenozoic

320 geodynamic evolution of the Tibet-Pamir orogen. Since the pioneering works of Burtman et al. (1963), Burtman

321 and Molnar (1993), Pan (1994), Mattern et al. (1996), Xiao et al. (2002) and references therein, the Kudi-Oytag

322 suture, or the "Paleozoic suture", has been hypothesized to be a single, once continuous, E–W-striking feature

323 that was bent towards the north by Cenozoic indentation of the Pamir into a postulated Tarim-Tajik block.

324 Recent publications outline an early Paleozoic history of the West Kunlun arc magmatism (Figure 9a). The

325 southward subduction of the Proto-Tethys started in the Terreneuvian, dated by the 531 Ma Nanpingxueshan

326 pluton in the Tianshuihai Group (Yin et al., 2020). As a consequence of the development of the Yixieke volcanic

327 arc (Xiao et al., 2005) and the Yierba arc, the South Kunlun was intruded by the Yierba adakitic diorite at ca.

328 513 Ma (Yin et al., 2020). In response to slab roll-back, the Kudi ophiolite formed in a back-arc position

329 between 513–516 Ma (Wang et al., 2021). The Proto-Tethys closed in the Silurian between 431–420 Ma (Wang

330 et al., 2020) with exhumation of metamorphic units starting from ca. 440 Ma, as dated by monazite U-Pb from

331 the Saitula Group (Zhang et al., 2018a). Closure of the Proto-Tethys was followed by the intrusion of A-type

post-orogenic granites, dated as 420–405 Ma by zircon U-Pb in the North Kudi granite (Yuan et al., 2002; Liu et al., 2014).

However, corresponding early Paleozoic geologic events or rock records in the North Pamir have not been reported. Instead, previous works on mafic to intermediate volcanic rocks and granitoids of the North Pamir show major subduction related arc magmatic activity in the mid to late Carboniferous (Rembe et al., 2021; Jiang et al., 2008; Ji et al., 2018; Kang et al., 2015; Ruzhentsev et al., 1977). Carboniferous arc magmatic rocks found in the Waqia (Tang et al., 2020) and East Mazar (Li et al., 2006) tectonic slivers, reflect the closure of a remnant ocean basin, whereas major arc magmatic activity was focused on the North Pamir arc further to the west (Figure 9b). Stratigraphic relations and hiati point to a soft collision and obduction of that North Pamir arc in the early Permian (Rembe et al., 2021). No broad Paleozoic magmatic activity younger than Lower Devonian is known in the West Kunlun. The Carboniferous North Pamir arc granitoids intrude largely into poorly dated mafic volcanic rocks. Our calcite U-Pb ages agree with the only known ages of this volcanic unit from Schwab et al. (2004) (Figure 8). They corroborate the dissimilarity of the West Kunlun and North Pamir arc volcanic rocks, and therefore argue against the existence of a continuous Paleozoic suture extending from the Pamir to the West Kunlun.

Recent studies on the Gissar and Kyzylkum segment of the South Tien Shan (STS) of Uzbekistan (Figure 1), West of the North Pamir document the presence of early Carboniferous metamorphism and constrain the volcanic age of meta-basalts from the northern Kyzylkum segment by zircon U-Pb dating to 320–300 Ma (Konopelko et al., 2019 and references therein). This is coeval with arc magmatic activity along the North Pamir arc. Konopelko et al. (2019) propose an archipelago model for the late Paleozoic suture zones in the STS, characterized by high-T metamorphism, rapid exhumation, and multiple subduction zones. This archipelago might have been connected to the Paleo-Tethys realm. We argue for a North Pamir arc continuing from the northeastern Pamir into the Tajik northwestern Pamir and the Gissar segment of the South Tien Shan.

6   Conclusion

Calcite phases in Paleozoic ocean floor volcanic rocks were studied with LA-ICP-MS. From four samples we investigated a total of 18 laser ablation areas. Three ablation areas yielded high quality lower intercept ages, 331 ± 15 Ma (17NP436a_A), 339 ± 17 Ma (17NP436b_A) and 328 ± 16 Ma (17NP436b_C), each with MSWD < 2 and propagated 2σ-error < 10%, which we interpret representing timing of individual geologic events. The majority of the remaining ablation area ages from volcanic breccia samples 17NP436a and 17NP436b as well as vesicular basalt sample 15NP233 overlap with this age within propagated 2σ-errors. They show slightly elevated MSWDs, implying that they are mixed ages. Sample 15NP236 has the most complex age results, possibly caused by more severe disturbance of the isotope ratios by younger events. Ages of samples 17NP436a, 17NP436b and 15NP233 agree with existing radiometric ages of correlative volcanic units in the North Pamir, demonstrating that calcite formed during ocean floor volcanism, due to coeval or subsequent ocean floor alteration, provides a valuable age constraint to the timing of volcanism. We note that these calcite ages do not directly date the formation of these volcanic rock but provide minimal age constraints within a timespan of about 25 Ma of ocean floor alteration.

369 Age data must be evaluated in the light of detailed petrographic analysis, including petrographic microscopy and
370 cathodoluminescence microscopy, as well as geochemistry of the investigated calcite. Geochemical data
371 supports our hypothesis of an ocean floor alteration related origin of the investigated calcite. However, we
372 underline that interpretation of REE content in calcite is not straight forward, since the trace element uptake by
373 calcite is dependent on a multitude of factors.

374 The presence of Middle to Upper Mississippian ocean floor in the North Pamir argues against models invoking a
375 continuous, early Paleozoic Kunlun belt, stretching from the West Kunlun far into the North Pamir. They support
376 the presence of a mid to late Carboniferous volcanic arc system, tying the North Pamir more to comparative units
377 in the Tien Shan.

7 Appendices

379 Appendix A: Reflected light images, Fig.A1–A4

380 Appendix B: X-ray fluorescence microscopy (XFM) maps, Fig. B1–6

381 Appendix C: REE data of each ablation area, Fig.C1

8 Code and data availability

383 Whole rock geochemistry data used from literature (Rembe et al. (2021), S1) as well as LA-ICP-MS isotope data
384 (S2) and geochemistry (S3) will be uploaded to UQ eSpace (https://espace.library.uq.edu.au/), run by the
385 University of Queensland, upon acceptance.

9 Author contribution

387 JR, RZ, ERS, and JK conceptualized the project. Fieldwork was carried out by JR, ERS, JK, and CJ.
388 Methodological concept preparation, Laboratory work and data interpretation was done by RZ, JR, JXZ, YF, and
389 DLH. JR prepared a first draft of the manuscript and all authors contributed to the review and editing procedure.

10 Competing interests

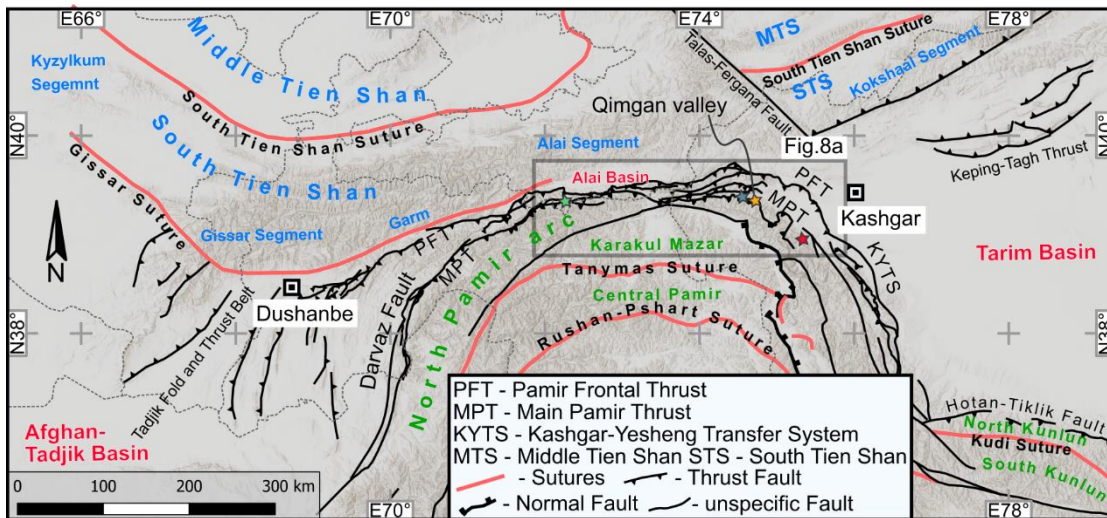391 All authors declare that they do not have any conflict of interest.

11 Acknowledgement

Figure 1: Overview map of the North Pamir and surroundings. The yellow star marks the position of the Qimgan valley, as noted. The meaning of the other star symbols is explained in Figure 8. Map drawn after Konopelko et al. (2019), Li et al. (2020), and Henan Institute of Geological Survey (2014).
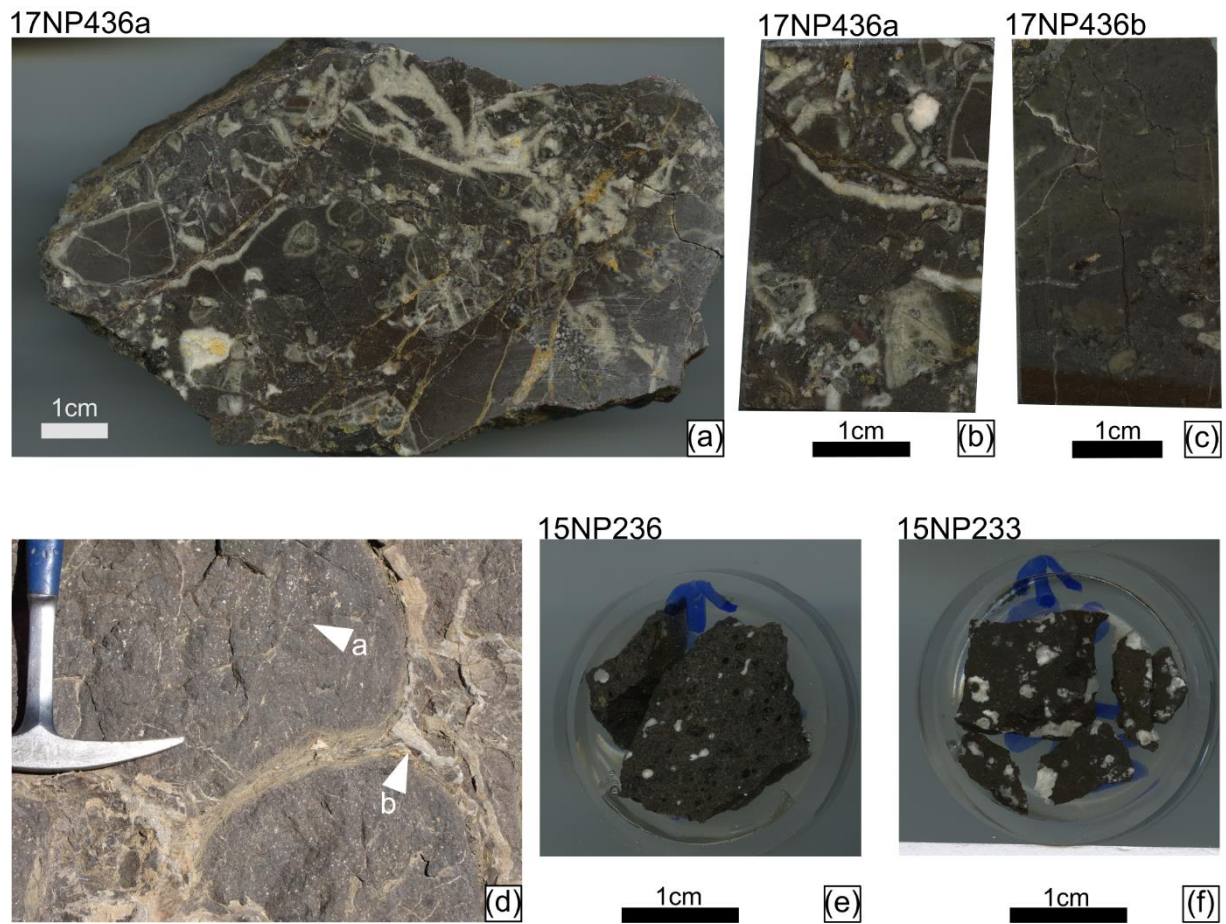
Figure 2: Sample photographs of hand specimen of sample 17NP436a (a) and polished rock block used for LA-ICP-MS measurements of sample 17NP436a (b) and 17NP436b (c). Field photograph of well-preserved amygdaloidal pillow-basalts in Oytag valley near Qimgan valley (d), with white arrows pointing at calcite filled vesicles (arrow a) and massive interstitial calcite (arrow b). Polished rock specimen 15NP236 (e) and 15NP233 (f) of similar rocks, were used for LA-ICP-MS.
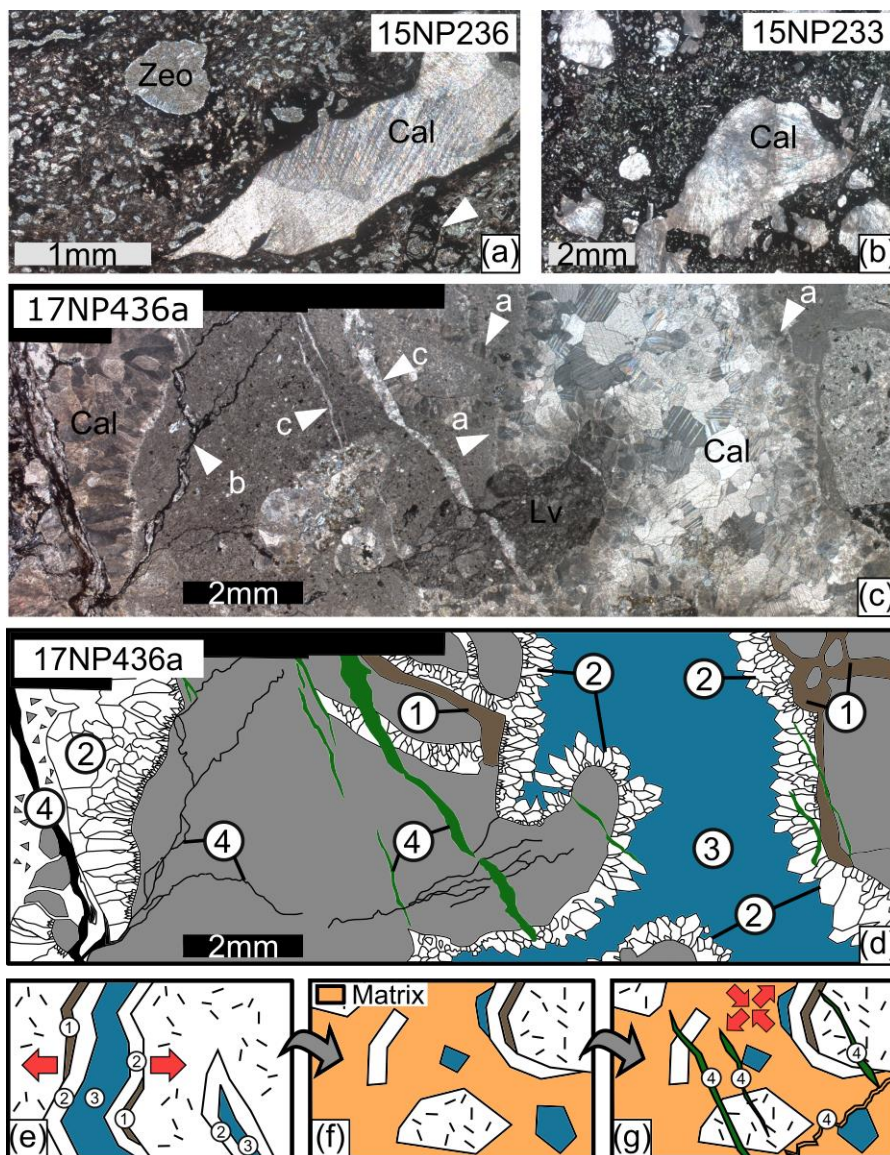
Figure 3: Typical calcite filled vesicles of sample 15NP236 (a), in this case with spary calcite and zeolite mineralization. The white arrow marks preserved perlitic structures. Botryoidal calcite was found in both amygdaloid-basalt samples, the example in (b) is from 15NP233. Figure 3c shows a thin section photograph of sample 17NP436a. White arrows indicate radial fibrous calcite (a), dark styloliths (b), calcite filled fissures (c). Figure 3a, b, c under crossed polarized light. Figure 3d shows a schematic sketch of microphotograph Figure 3c, delineating a sequence of 4 events: (1) formation of hydrothermal clay, (2) precipitation of fibrous-radial calcite along the walls of brecciated volcanic rock fragments, (3) late-stage equant calcite formation, (4) pressure solution and formation of styloliths (dark lines) and reprecipitation of dissolved calcite in fissures (green). Areas 2 and 3 are targets for laser ablation. In figures (e)-(f) a schematic sequence of events leading to the formation of the basaltic breccias is sketched. (e) Fracturing of the basaltic rock and formation of clay (1) and calcite cement phases (2) and (3). (f) disarticulation and sedimentation of debris containing isolated calcite cement fragments. (g) late stage pressure solution and fissure formation of phase (4). Red arrows schematically mark stress regime.
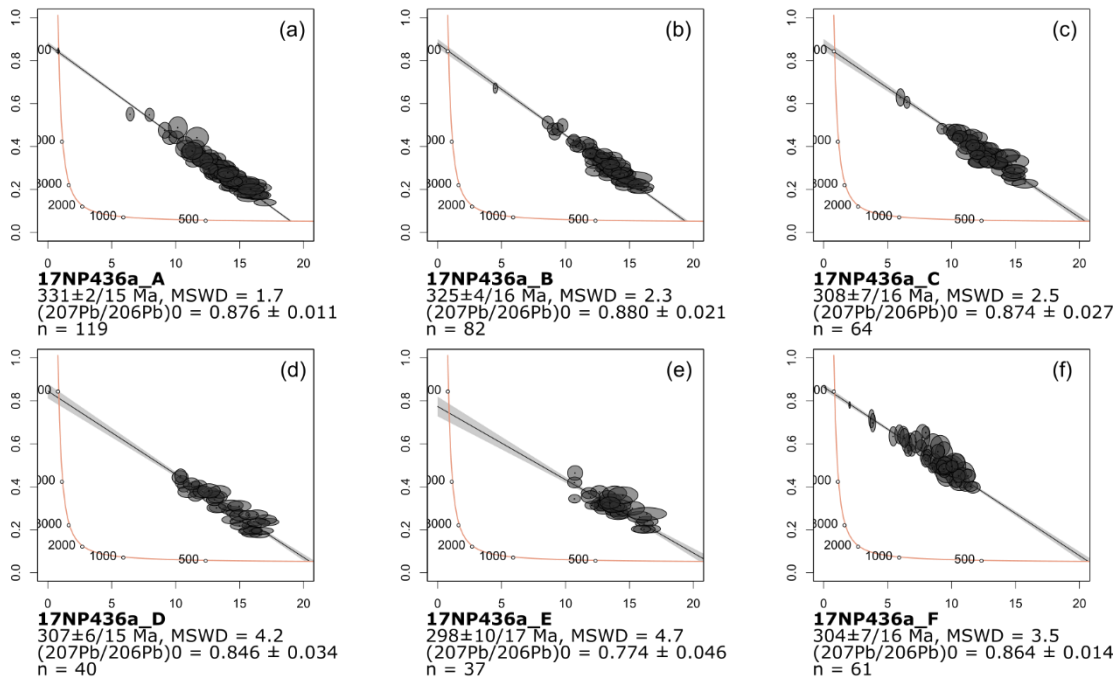
15

430
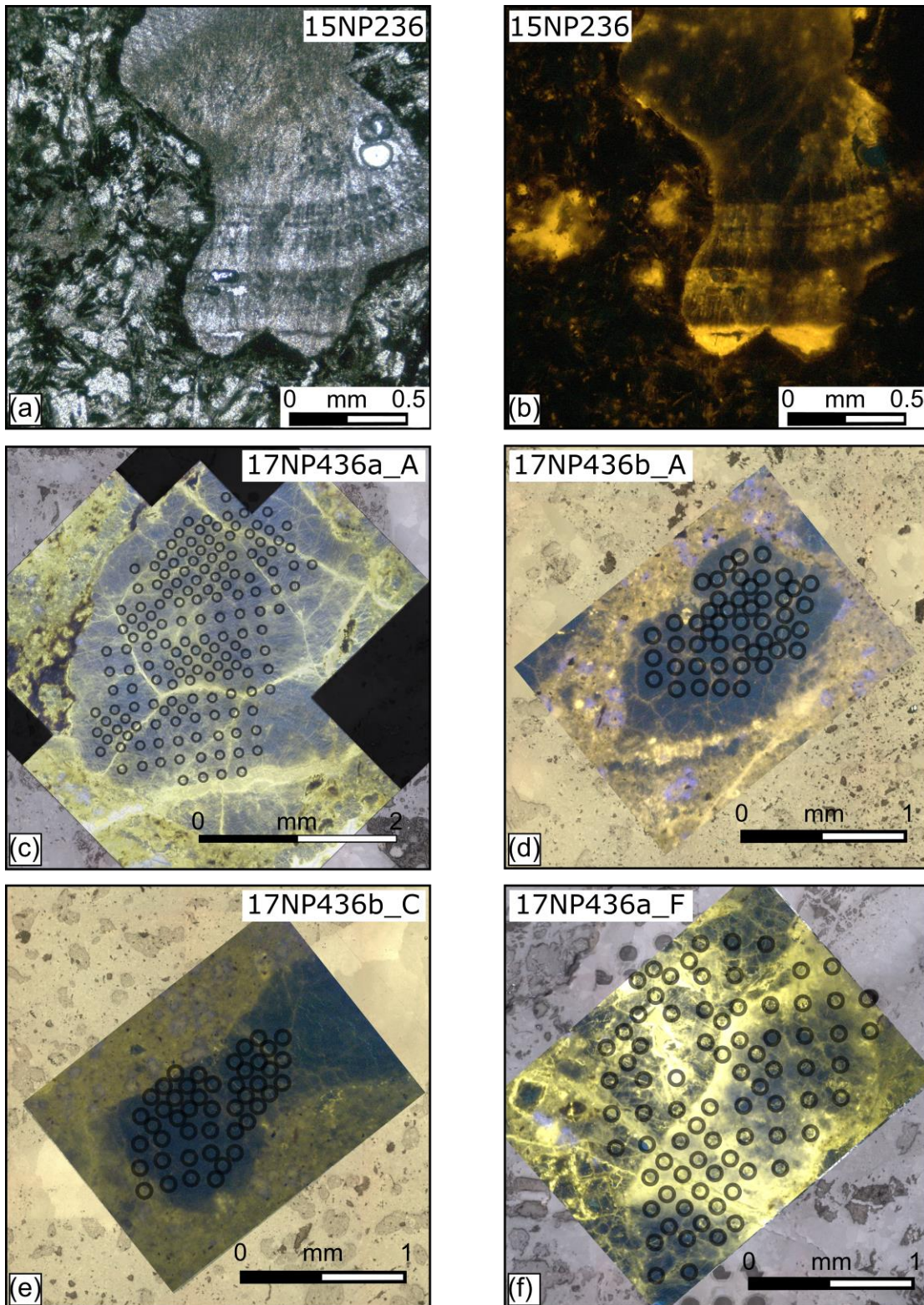
Figure 4: Microphotographs under plain light (a) and Cathodoluminescence (b) of an exemplary vesicle of sample 15NP236 show primary botryoidal structure of the calcite. Primary calcite seems non-luminescent to dull-luminescent. Cathodoluminescence images of ablation areas 17NP436a_A (c), 17NP436b_A (d) and 17NP436b_C (e) show relatively homogenous non-luminescent calcite cement fragments with a small portion of bright yellow veins. The calcite cement fragments are embedded in a dull-yellow luminescent volcaniclastic matrix. All three samples yielded high quality calcite U-Pb ages (MSWD < 2). Ablation area 17NP436a_F (f), which has a high portion of bright yellow calcite, yielded a less precise age (MSWD = 3.5). Ablation spots for geochemistry and U-Pb dating are marked with grey circles.

438

Basalt breccia sample 17NP436a

17NP436a_A
331±2/15 Ma, MSWD = 1.7
$(207Pb/206Pb)0 = 0.876 \pm 0.011$
n = 119

17NP436a_B
325±4/16 Ma, MSWD = 2.3
$(207Pb/206Pb)0 = 0.880 \pm 0.021$
n = 82

17NP436a_C
308±7/16 Ma, MSWD = 2.5
$(207Pb/206Pb)0 = 0.874 \pm 0.027$
n = 64

17NP436a_D
307±6/15 Ma, MSWD = 4.2
$(207Pb/206Pb)0 = 0.846 \pm 0.034$
n = 40

17NP436a_E
298±10/17 Ma, MSWD = 4.7
$(207Pb/206Pb)0 = 0.774 \pm 0.046$
n = 37

17NP436a_F
304±7/16 Ma, MSWD = 3.5
$(207Pb/206Pb)0 = 0.864 \pm 0.014$
n = 61

Basalt breccia sample 17NP436b

17NP436b_A
339±6/17 Ma, MSWD = 1
$(207Pb/206Pb)0 = 0.974 \pm 0.100$
n = 38

17NP436b_B
322±3/15 Ma, MSWD = 4.8
$(207Pb/206Pb)0 = 0.866 \pm 0.017$
n = 47

17NP436b_C
328±4/16 Ma, MSWD = 1.7
$(207Pb/206Pb)0 = 0.893 \pm 0.045$
n = 29

17NP436b_D
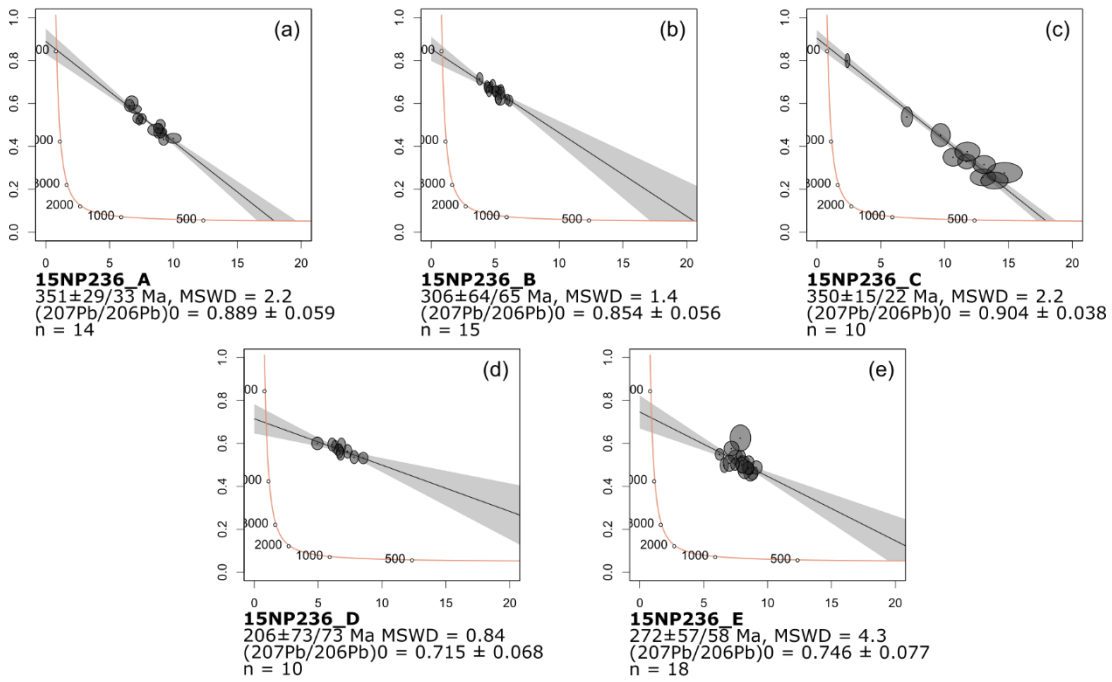316±9/17 Ma, MSWD = 2.4
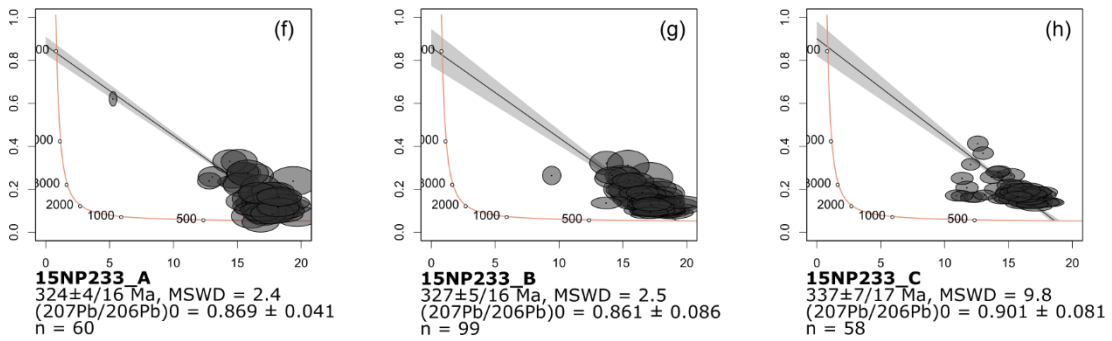$(207Pb/206Pb)0 = 0.830 \pm 0.058$
n = 23

439

440 *Figure 5: Tera-Wasserburg plots of ablation area ages on basalt breccia samples 17NP436a and 17NP436b. All errors are*
441 *given as 2σ.*

442

Vesicular basalt sample 15NP236

15NP236_A
351±29/33 Ma, MSWD = 2.2
(207Pb/206Pb)0 = 0.889 ± 0.059
n = 14

15NP236_B
306±64/65 Ma, MSWD = 1.4
(207Pb/206Pb)0 = 0.854 ± 0.056
n = 15

15NP236_C
350±15/22 Ma, MSWD = 2.2
(207Pb/206Pb)0 = 0.904 ± 0.038
n = 10

15NP236_D
206±73/73 Ma MSWD = 0.84
(207Pb/206Pb)0 = 0.715 ± 0.068
n = 10

15NP236_E
272±57/58 Ma, MSWD = 4.3
(207Pb/206Pb)0 = 0.746 ± 0.077
n = 18

Vesicular basalt sample 15NP233

15NP233_A
324±4/16 Ma, MSWD = 2.4
(207Pb/206Pb)0 = 0.869 ± 0.041
n = 60

15NP233_B
327±5/16 Ma, MSWD = 2.5
(207Pb/206Pb)0 = 0.861 ± 0.086
n = 99

15NP233_C
337±7/17 Ma, MSWD = 9.8
(207Pb/206Pb)0 = 0.901 ± 0.081
n = 58

Figure 6: Tera-Wasserburg plots of ablation area ages on vesicular basalt samples 15NP236 and 15NP233. All errors are given as 2σ.
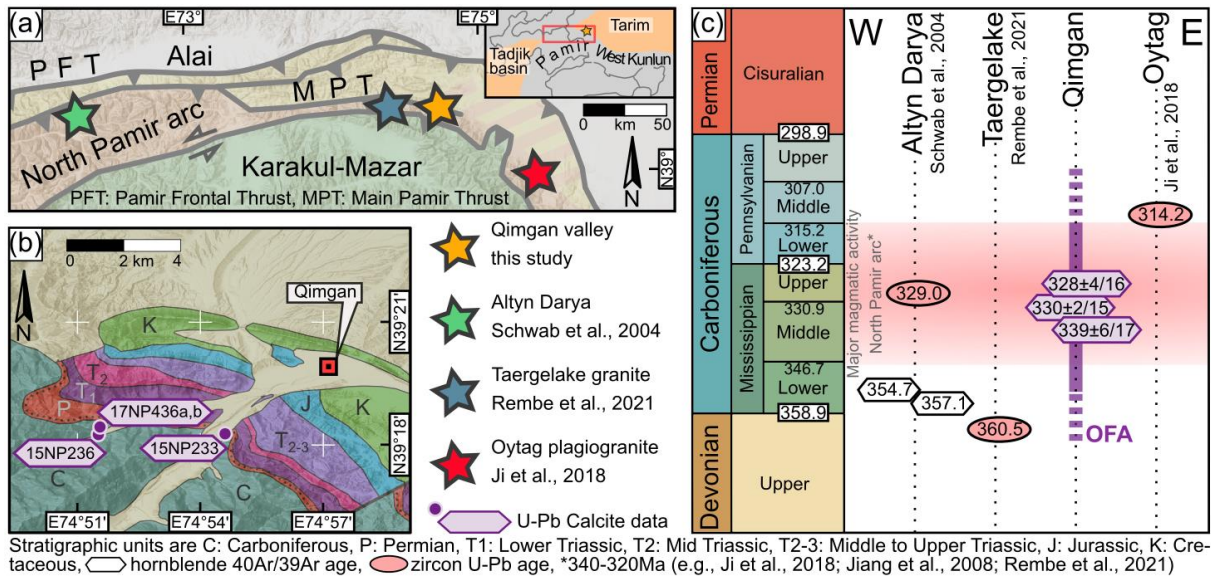
18
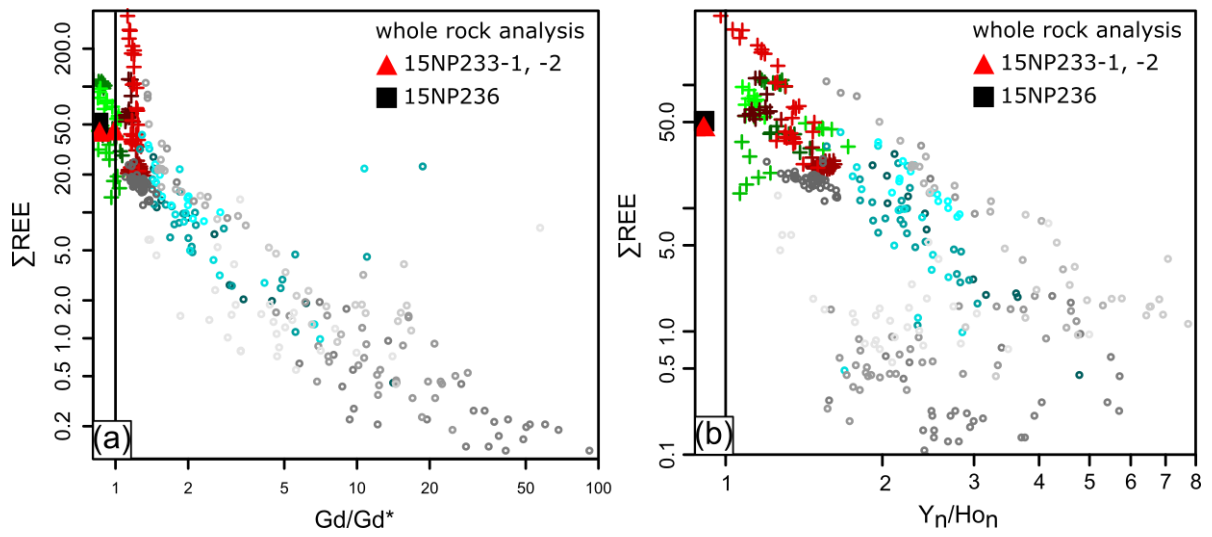
447

448 *Figure 7: (a) Mixing trend between high total REE—negative Gd/Gd* and low total REE—positive Gd/Gd* composition. (b)*

449 *Higher Y_n/Ho_n values correlate with low total REE. Y and Ho normalized against chondrite values of Anders and Grevesse*

450 *(1989). (e, f) + -15NP233, -236, o -17NP436A, -B; color-code see Appendix A.*

451

452 Stratigraphic units are C: Carboniferous, P: Permian, T1: Lower Triassic, T2: Mid Triassic, T2-3: Middle to Upper Triassic, J: Jurassic, K: Cretaceous, ⬭ hornblende 40Ar/39Ar age, ⬭ zircon U-Pb age, *340-320Ma (e.g., Ji et al., 2018; Jiang et al., 2008; Rembe et al., 2021)

453 *Figure 8: (a) Map of the northeastern Pamir with location of radiometric ages for the North Pamir arc volcanic rocks,*

454 *shown in c. (b) Detailed field locations of samples in the Qimgan valley (map after Henan Institute of Geological Survey*

455 *(2014)). There is a sedimentary hiatus between the Middle Pennsylvanian and the Guadalupian (Rembe et al., 2021). (c)*

456 *Overview of selected literature data and newly obtained data for OFA of the North Pamir Carboniferous arc.*

457

458
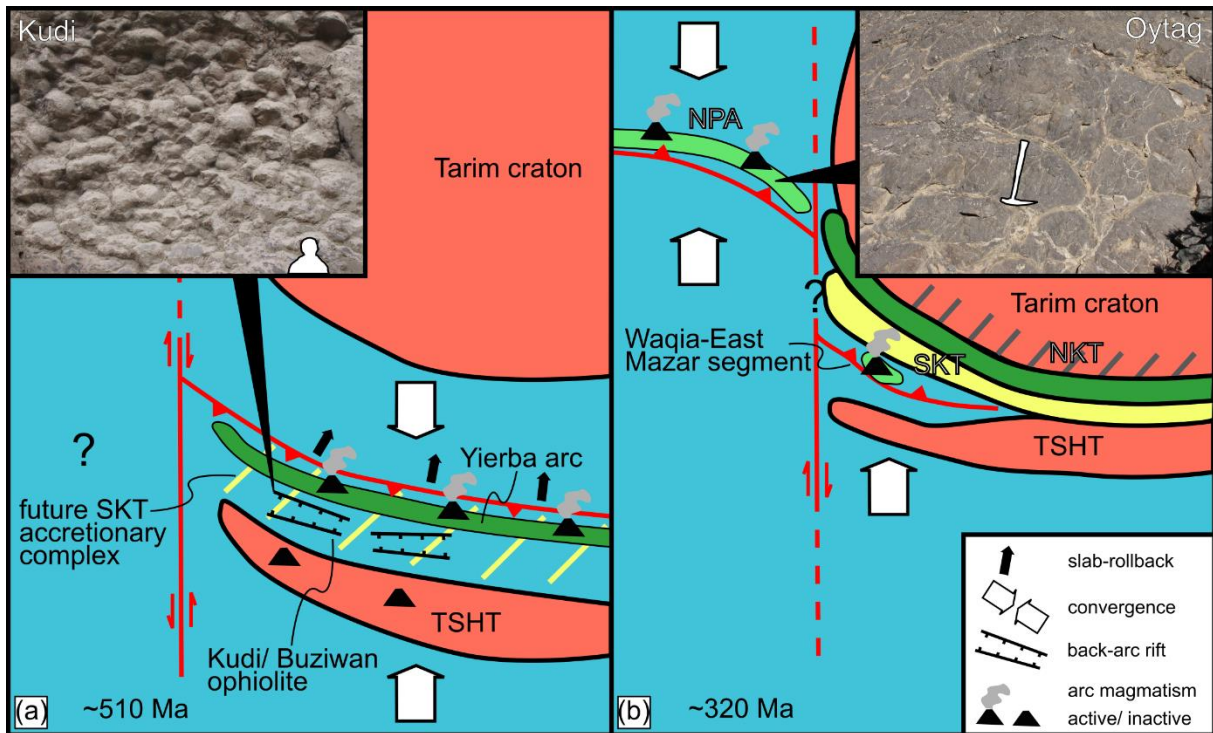
Figure 9: (a) Paleogeographic situation in the mid-Cambrian: The roll-back of the Proto-Tethys slab caused the formation of

the Kudi ophiolite, exposed in the Buziwan valley (Wang et al., 2021). (b) Paleogeographic situation in the late

Mississippian: The North Pamir arc formed along an intra-oceanic subduction zone (Jiang et al., 2008) forming the Oytag

segment in its eastern branch. Subduction related Waqia granite (Tang et al., 2020) and East Mazar granite (Li et al., 2006),

both today part of tectonic slivers, suggest the presence of a remnant oceanic basin between Tianshuihai and South Kunlun

Terrane accretionary complex, as suggested by (Zhang et al., 2018b). Small photographs show pillow basalts in the Kudi

section (in a) and Oytag near Qimgan (in b). SKT-South Kunlun Terrane, TSHT-Tianshuihai Terrane, NPA-North Pamir
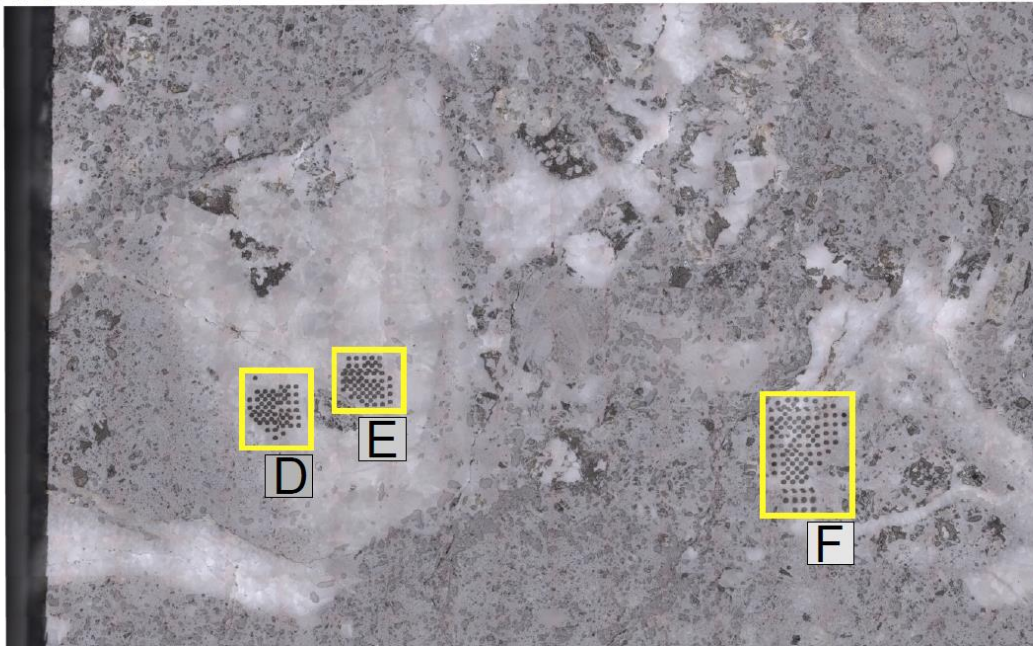
volcanic arc, NKT-North Kunlun Terrane.

13 REFERENCES

469 Jiang, C. F.: Opening-closing tectonics of Kunlun Mountains, Geol. Memoirs. MGMR, 12, 1–224, 1992.
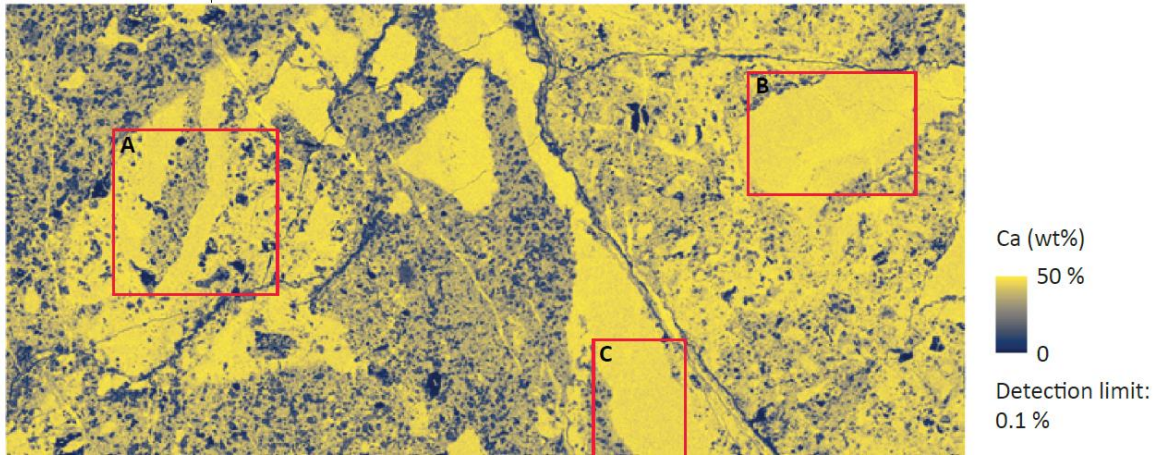470

17NP436a

471

Appendix A: Reflected light images of all investigated samples with marked ablation areas. Letter, attached to the yellow boxes, appended to the sample name, labels the ablation areas. Colors of label boxes are consistent with colors of in-text figures.

475

Scan 66079 (resolution: 10 μm/pixel; dwell time: 1 ms)

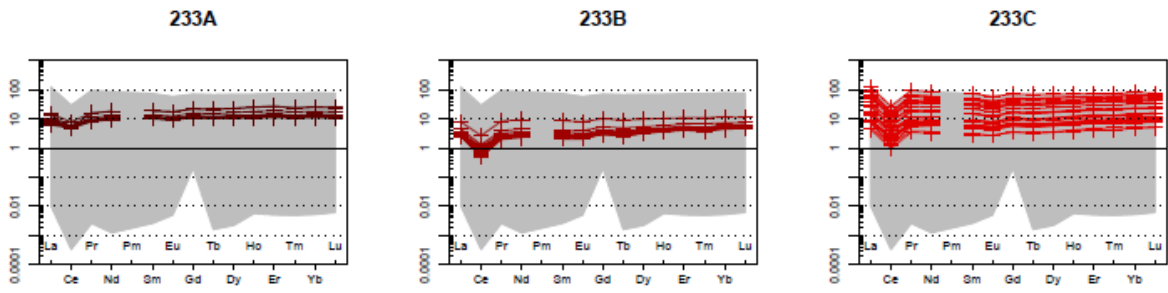Ca (wt%)

50 %

0

Detection limit:
0.1 %

476

477   *Appendix B: XFM Map*

478

Spider plot − REE chondrite (Boynton 19

233A

233B

233C

479

480 *Appendix C: Overview REE data per ablation area*

481

Appendix 1: Whole rock geochemistry from Rembe et al., 2021					
sample number	locality	field description	SiO2	TiO2	Al2O3
			(%)	(%)	(%)
15NP233-1	Qimgen - Akqiy	Basalt	37.7	0.842	13.3
15NP233-2	Qimgen - Akqiy	Basalt	37.7	0.843	13.3
15NP236	Qimgen - Akqiy	pillow basalt	38.5	0.928	14.0

482

483 *Supplementary Table 1: Whole rock geochrmistry*

484

Source file	238_206	2S_238_206	207_206	2S_207_206
17NP436a_Ag001	14.1948	1.0272	0.2440	0.0180
17NP436a_Ag002	12.6732	0.9530	0.3180	0.0220
17NP436a_Ag003	13.0222	1.0094	0.2780	0.0210
17NP436a_Ag004	11.5790	0.9292	0.3720	0.0270
17NP436a_Ag005	15.8192	1.1015	0.1920	0.0150
17NP436a_Ag006	14.7784	1.0533	0.2530	0.0180
17NP436a_Ag007	15.5186	1.0323	0.1750	0.0130
17NP436a_Ag008	10.9979	0.7913	0.3750	0.0260
17NP436a_Ag009	12.2582	0.8926	0.3310	0.0220
17NP436a_Ag010	9.5385	0.7132	0.4430	0.0270

485

486   *Supplementary Table 2: LA-ICP-MS age data.*

487

sample num	locality	group	symbol	color	size	MnO	Ba	Sr	Zr	Y	La
NP236_Ag01	Qimgen - Ak	236A	3	10	1.3	0.093	0.71	314.47	1.26	21.11	5.2
NP236_Ag03	Qimgen - Ak	236A	3	10	1.3	0.028	1.07	385.76	0.86	20.44	3.98
NP236_Ag04	Qimgen - Ak	236A	3	10	1.3	0.087	1.13	311.39	0.35	12.07	1.96
NP236_Ag05	Qimgen - Ak	236A	3	10	1.3	0.313	14.54	315.15	0.24	14.82	2.19
NP236_Ag06	Qimgen - Ak	236A	3	10	1.3	0.098	138.83	953.86	0.66	16.72	2.77
NP236_Ag10	Qimgen - Ak	236A	3	10	1.3	0.05	1.17	343.03	0.79	19.45	4.42
NP236_Ag11	Qimgen - Ak	236A	3	10	1.3	0.01	0.45	449.24	0.56	17.49	5.71
NP236_Ag12	Qimgen - Ak	236A	3	10	1.3	0.047	0.75	382.22	0.77	18.44	4.76
NP236_Ag13	Qimgen - Ak	236A	3	10	1.3	0.025	1.27	361.14	0.87	20.55	3.84
NP236_Bg01	Qimgen - Ak	236B	3	17	1.3	0.025	1.08	366.4	1.05	41.18	12.33

Supplementary Table 3